Glacial erosion model

The ice thickness, h, is computed by solving the equation of mass conservation (Cuffey and Paterson 2010):

$$\frac{\partial h}{\partial t} = M - \nabla \cdot \mathbf{q} \quad (1)$$

where $\mathbf{q}$ is the vertically averaged ice flux ($\mathbf{q}=h\mathbf{u}$, where $\mathbf{u}$ is the vertically integrated horizontal ice velocity) and M the surface mass balance. The ice velocity, $\mathbf{u}$, is the sum of the deformation and the sliding velocities. The shallow ice approximation is used (Mahaffy 1976, Hutter 1983) to compute Equation 1 with efficiency,

$$\frac{\partial h}{\partial t} = M - \nabla \cdot \left[\left(\frac{2B}{n+2}(\rho g)^n h^{n+2} + B_s (\rho g)^n h^n\right)|\nabla(h+z)|^{n-1}\nabla(h+z)\right] \quad (2)$$

where B is the ice flow-law parameter ($6.8\text{x}10^{-24}$ $\text{Pa}^{-3}\text{s}^{-1}$), B_s the sliding law parameter ($3.4\,\text{x}10^{-18}$ $\text{Pa}^{-3}\text{m}^2\text{s}^{-1}$), ρ the density of the ice (910 kg/m), g the gravitational acceleration (9.81 m/s), n Glen's Flow parameter (3), and z the bedrock topography. Equation 2 is solved using the finite difference method. The model is run until steady state is reached. We use the GEBCO One Minute Grid digital elevation model for the topography, which was re-interpolated at a 5 km resolution to make sure the shallow ice approximation remains valid. The sliding velocity, $\mathbf{u_s}$, is then calculated

$$\mathbf{u_s} = B_s (\rho g)^n h^{n-1}|\nabla(h+z)|^{n-1}\nabla(h+z) \quad (3)$$

where the temperature of the ice at the ice-bedrock interface is at melting point (see below for the treatment of the temperature). Finally, erosion rates are computed as follows

$$\dot{e} = K_g|\mathbf{u_s}|^l \quad (4)$$

where $\dot{e}$ is the erosion rate, K_g is an erosion constant ($5\text{x}10^{-5}$) and l the erosion law exponent set equal to 1 (Humphrey and Raymond 1994).

Finally, we reduce the complexity of the model to concentrate on the effects of precipitation and temperature. The model does not include calving or a grounding line, which may modify the model extent, particularly for the western regions. Our goal is solely to highlight the impact of a shift of southern Westerly winds and its effect on precipitation using a simple model. We show that higher precipitation rates about 44°S are required to explain the ice extent. It implies higher flux and higher erosion rates.

Ice surface mass balance calculation

The surface mass balance model is specified using an empirical parameterization (Oerlemans 1997, Giesen and Oerlemans 2012), with mass gain resulting from snow precipitation, P_s, and mass loss due to the surface energy balance, Q, and is computed as follows

$$M = \int P_s + \min(0, \frac{-Q}{\rho_w L_f}) \, dt \quad (5)$$

where ρ_w is the density of water (1000 kg/m^3) and L_f (3.34x10^5 J/Kg) is the latent heat of fusion. Q is computed as follows

$$Q = \max(-25, -25 + 20 \, T_s) \quad (6)$$

where T_s is the surface temperature (see treatment of temperature below). Total precipitation accounts for changes in altitude and Westerly wind direction through a heuristic parameterization of orographic precipitation,

$$P = \left[\frac{C_0 - \int_0^x P(x')dx'}{C_1}\right] z \quad (7)$$

where

$$C_0 = \alpha e^{-\left|\frac{y-y_p}{\phi}\right|} + 3\text{x}10^5 \quad (8)$$

in which y is the distance along the latitudinal direction, C_1 is a constant (0.25x10^8 m^2) and ϕ sets the width of peak precipitation (150 km). y_p is chosen such that peak precipitation is centered about 44°S in the first two experiments, and about 50°S in the third one. α is an *ad hoc*, adjustable parameter that

controls the magnitude of precipitation. It is set to $9x10^6$ m^2/yr in the first experiment, $3x10^6 m^2/yr$ in the second and $2.5x10^6$ m^2/yr in the third one. The difference in precipitation between the first and third simulation is slightly higher than the 2-fold increase suggested in the literature (Moreno et al. 1999, Rojas et al. 2009). However, α was adjusted to produce comparable max accumulation rates for both simulations. Keeping high precipitation rates by setting α to $4.5x10^6$ m^2/yr in the third simulation leads to accumulation rates higher than 10 m/yr because of the energy term in the mass balance model (Equation 5). It produces an even larger ice sheet in the southern parts of the model, but it leads to the same conclusions.

Precipitation only falls as snow (P_s) where T_s is less than 2°C (Auer 1974). We assume wind comes from the west, although in reality it was more likely coming in a northwest direction. Ultimately, M is filtered using a local regression method and then shifted 30 km to the west to resemble mass balance typically observed on large ice sheets and to better fit the ice extent. The resulting ice mass balance is shown in Figure DR1. We also show in Figure DR2, the distributions of ice thickness, surface temperature and mass balance estimate for Experiment 1 (Figure 2a and Figure DR1a).

Surface and basal temperature

The ice surface and basal temperatures are required to compute the mass balance and estimate where the ice is sliding, or not sliding. Annual surface temperature accounts for altitudinal and latitudinal variations and is computed as follows

$$T_s = T_0 - \gamma_1 y - \gamma_2 (z + h) \quad (9)$$

where γ_1 is the latitudinal temperature gradient ($5.9x10^{-6}$ °C/m), γ_2 the altitudinal lapse rate ($5x10^{-3}$ °C/m) and T_0 the temperature at sea level in the top left corner of the model domain (see calculation below). The basal temperature is computed using a 1D analytical solution of the heat transfer equation (Robin 1955, Clarke et al. 1977). In the accumulation area, the basal temperature is given by

$$T_b = T_s + \frac{q}{k}\sqrt{\frac{\pi h \kappa}{2M}}\,\mathrm{erf}\left[\sqrt{\frac{hM}{2\kappa}}\right] \quad (10)$$

and in the ablation area by

$$T_b = T_s + h\,\frac{q}{k}\int_0^1 e^{\frac{hM}{2\kappa}(1-\xi)^2}\,d\xi \quad (11)$$

where q is the surface heat flow (70 mW.m^{-2}), k is the thermal conductivity of the underlying bedrock (2.35 W/(mK)) and κ is the thermal diffusivity of ice (1.22x10^{-6} m^2/s). Note, this is not an accurate model for ice temperature because the ice cannot exceed the melting point and horizontal conduction and advection are ignored**.** Sliding is computed where T_b is greater than the melting temperature T_m,

$$T_m = -8.7\ 10^{-4}\ h \quad (12)$$

Finally, we use the Precis-DFG climate data to calculate T_0 at the LGM. This is a 0.25° gridded data set including precipitation, surface temperature, surface humidity, and wind speed and direction for the period 1960-1990. It currently shows a mean annual temperature of about 15 °C at 40°S. Assuming that the mean annual temperature was about 5 to 6°C lower during glacial maxima (e.g. Porter 1981, Clapperton 1994, Hulton et al. 1994), we set T_0 equal to 9.4°C at 40°S. The resulting basal conditions (i.e. frozen- vs. warm-based) are shown in Figure DR3.

To further assess the whether the ice was frozen to its bed in the southern Patagonian Andes, we ran three additional simulations in which vary T_0, keeping all other parameters constant to Experiment 1. The results are shown in Figure DR4. It shows it was unlikely that the ice was frozen in valleys during glacial maxima.

Data compilation

The compilation of thermochronometric data includes published apatite (U-Th)/He, apatite fission track, zircon (U-Th)/He and zircon fission track ages. We modified data compared to the available global database (Herman et al. 2013),

including corrections for mislocated samples and screened for samples that may have been affected by recent volcanic activity. Finally, we included Al-in hornblende geobarometry data (Hervé 1995, Seifert et al. 2005, Leuthold et al. 2012). In that case, we only used the depth of emplacement and associated age in the inversion approach described below. The data are shown in Figure DR5.

Inversion of thermochronometric data

We use a modified version of the method recently developed by Fox et al. (2014), and used in Herman et al. (2013), to invert thermochronometric datasets. This method exploits the information contained in both age-elevation profiles and multi-thermochronometric systems strategies. In this approach, the depth to the closure temperature is expressed as the integral of erosion rate from the thermochronometric age to present-day,

$$z_c = \int_0^{\tau} \dot{e}\ dt \tag{13}$$

where z_c is the closure depth, τ is the thermochronometric age and $\dot{e}$ the erosion rate. To impose a positivity constraint on our inverse problem, we perform a change of variable in the logarithmic space where

$$\zeta = \ln(z_c) \tag{14}$$

$$\varepsilon = \ln(\dot{e}) \tag{15}$$

which we include in Equation 13 that becomes

$$\zeta = \ln\left(\int_0^{\tau} \exp(\varepsilon)\, dt\right) \tag{16}$$

This forms the inverse problem we wish to solve for ε. This can be achieved given that ζ is estimated. To compute ζ, we first compute z_c using the same method as described in detail in Fox et al. (2014), and then take the logarithm of the solution. This inverse problem is weakly non-linear and can be solved using the least-squares method (e.g. Tarantola 2005). We achieve this by first discretizing the integral in Equation 16. It then becomes a summation in which the erosion rate (i.e. exponential of ε) is parameterized as a piecewise constant function over fixed time intervals. Similarly to Fox et al. (2014), we impose the

condition that ε is correlated in space by defining an a priori model covariance matrix, $\mathbf{C_M}$. This matrix is constructed for all time intervals using the horizontal distance between the *ith* and *jth* data points, *d*, and a Gaussian correlation function,

$$C_M(\mathrm{i,j}) = \sigma^2 \exp\left(-\left(\frac{d}{L}\right)^2\right) \tag{17}$$

where *L* is a specified correlation length, *d* the distance between samples, and σ^2 is the a priori variance, which serves primarily as a weighing factor. It is worth noting that this covariance matrix simply implies that samples close to each other must follow the same erosion history and that samples far apart follow independent histories. Finally, both the temperature field and closure depth calculations depend on the solution (i.e. estimated erosion rates), which implies a second non-linearity (Fox et al. 2014).

The non-linear problem is solved using the steepest descent algorithm (Tarantola 2005, p.70),

$$\boldsymbol{\varepsilon_{m+1}} = \boldsymbol{\varepsilon_m} + \mu\left(\mathbf{C_M G^t C_D^{-1}}(\boldsymbol{\zeta_m} - \boldsymbol{\zeta_{obs}}) + (\boldsymbol{\varepsilon_m} - \boldsymbol{\varepsilon_{pr}})\right) \tag{18}$$

where *m* is the number of iterations, $\mathbf{C_D}$ is the data covariance matrix (which is a diagonal matrix) and μ is an *ad hoc* parameter chosen by trial and error. The model and data covariance are chosen to minimize tradeoff between model and data variance, σ_d^2 , (e.g. Aster et al. 2012) (σ_d = 0.6, L=30 km and $\sigma = 1.8$). We start the iterative process using the a priori expected value of ε_{pr} ($\varepsilon_{pr} =$ ln (0.4)) and *G* corresponds to:

$$G(i,j) = \frac{\partial \ln\left(\sum \exp(\varepsilon)\,\Delta t\right)}{\partial \varepsilon_j} \tag{19}$$

which can be computed analytically,

$$G(i,j) = \frac{\exp(\varepsilon_j)\,\Delta t}{z_{c,j}} \tag{20}$$

Ultimately, the erosion rates, $\dot{e}$, are computed by taking the exponential of ε.

163 The misfit function, *S*, that we minimize during the iterative process (Figure
164 DR6) corresponds to

165 $$2S(\boldsymbol{\varepsilon}) = (\boldsymbol{\zeta_m} - \boldsymbol{\zeta_{obs}})^t \boldsymbol{C_D^{-1}} (\boldsymbol{\zeta_m} - \boldsymbol{\zeta_{obs}}) + (\boldsymbol{\varepsilon_m} - \boldsymbol{\varepsilon_{pr}})^t \boldsymbol{C_M^{-1}} (\boldsymbol{\varepsilon_m} - \boldsymbol{\varepsilon_{pr}}) \quad (21)$$

166 Finally, the posterior covariance, $\widetilde{\boldsymbol{C}}$, corresponds to

167 $$\widetilde{\boldsymbol{C}} = \mathbf{C_M} - \mathbf{C_M} \mathbf{G}^{\boldsymbol{t}} (\mathbf{G} \mathbf{C_M} \boldsymbol{G^t} + \mathbf{C_D})^{-1} \mathbf{G} \mathbf{C_M} \quad (22)$$

168 where the diagonal elements of $\widetilde{\boldsymbol{C}}$ give the a posteriori variance, ${\sigma_{po}}^2$ (Figure
169 DR7). The a posteriori variance is a measure of the uncertainty on the parameter
170 estimate with respect to the a priori variance. The ratio between a priori and a
171 posteriori variance indicates whether the inclusion of data allows gaining
172 information on the estimated exhumation rate.

173

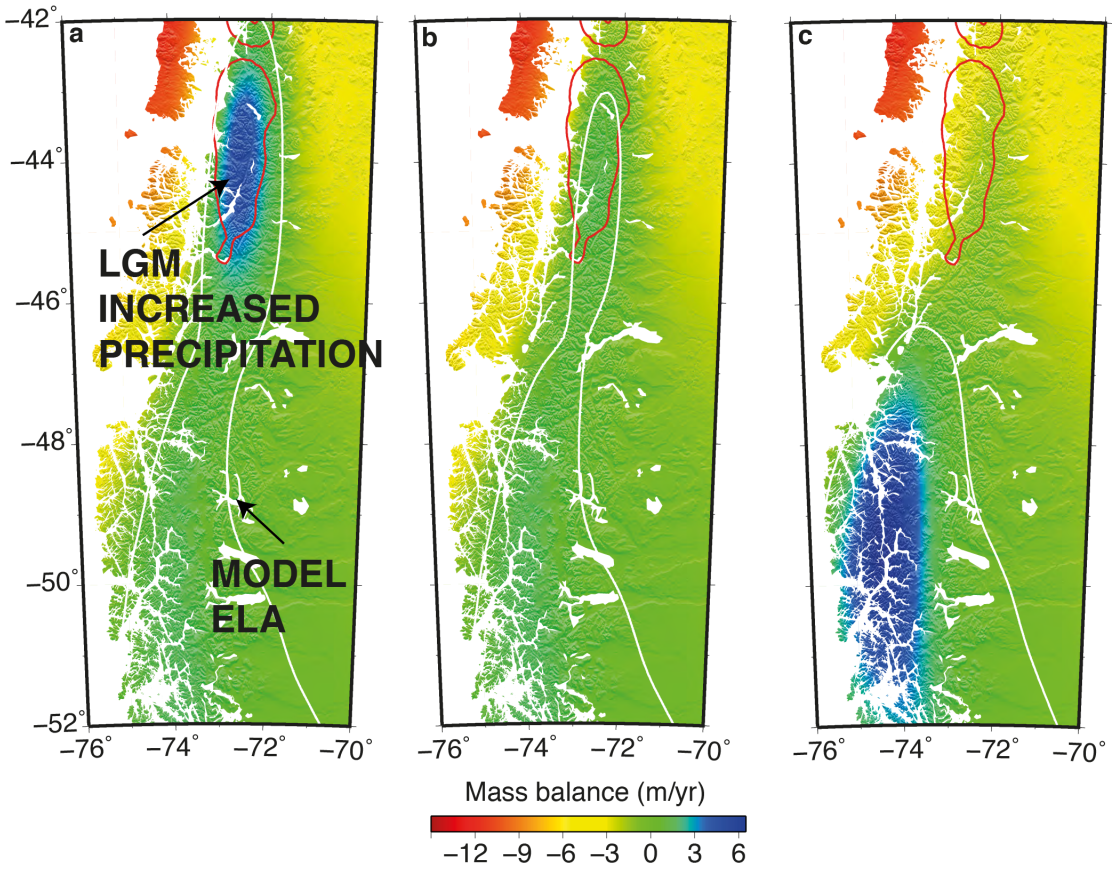

174

175 **Figure DR1. Prescribed mass balance. (a)** Prescribed surface mass balance
176 from Experiment 1, **(b)** for Experiment 2 and **(c)** for Experiment 3. The blue zone
177 in **(a)** highlights the effect of increased precipitation on the surface mass balance.
178 Red contours highlight the region where erosion rates are higher than 0.6
179 mm/yr (i.e. erosion hotspot) in the inversion results shown in Figure 4.

180

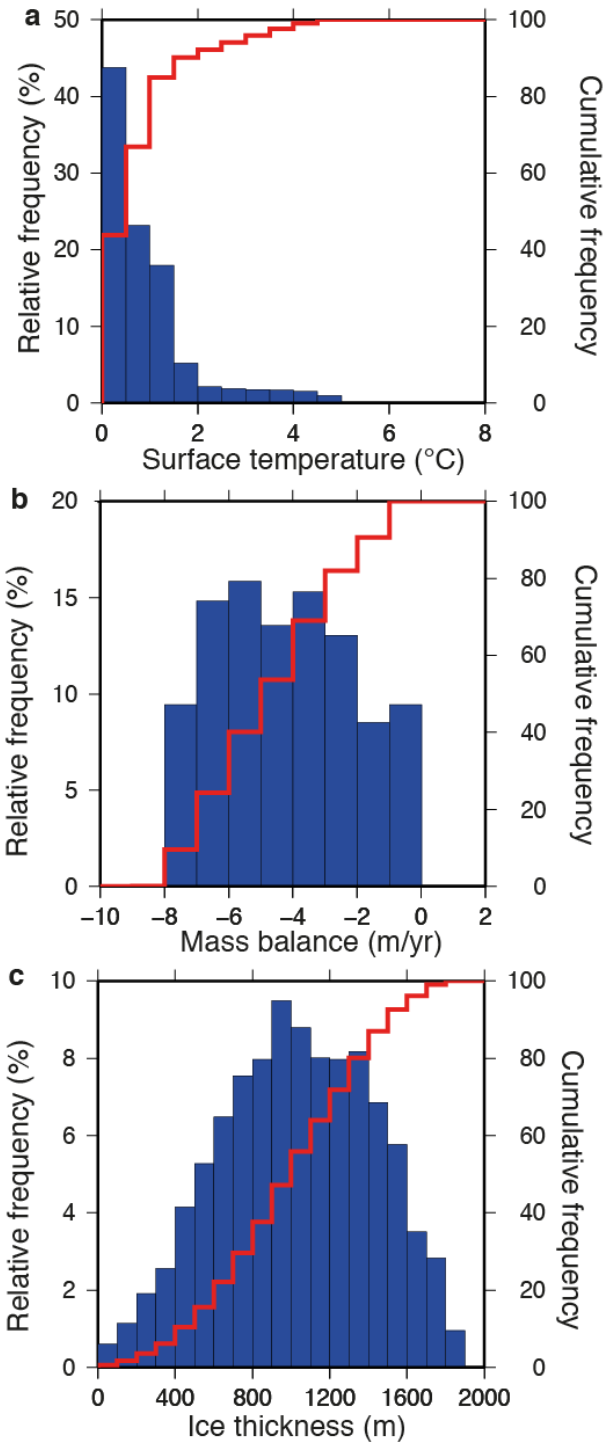

Figure DR2. Distribution of ice thickness, surface temperature and mass balance for Experiment 1. Relative frequency (blue bars) and cumulative distribution (red line) for **(a)** surface temperature, **(b)** accumulation rate and **(c)** ice thickness in the accumulation area for the ice model shown in Figure 2a (Experiment 1).

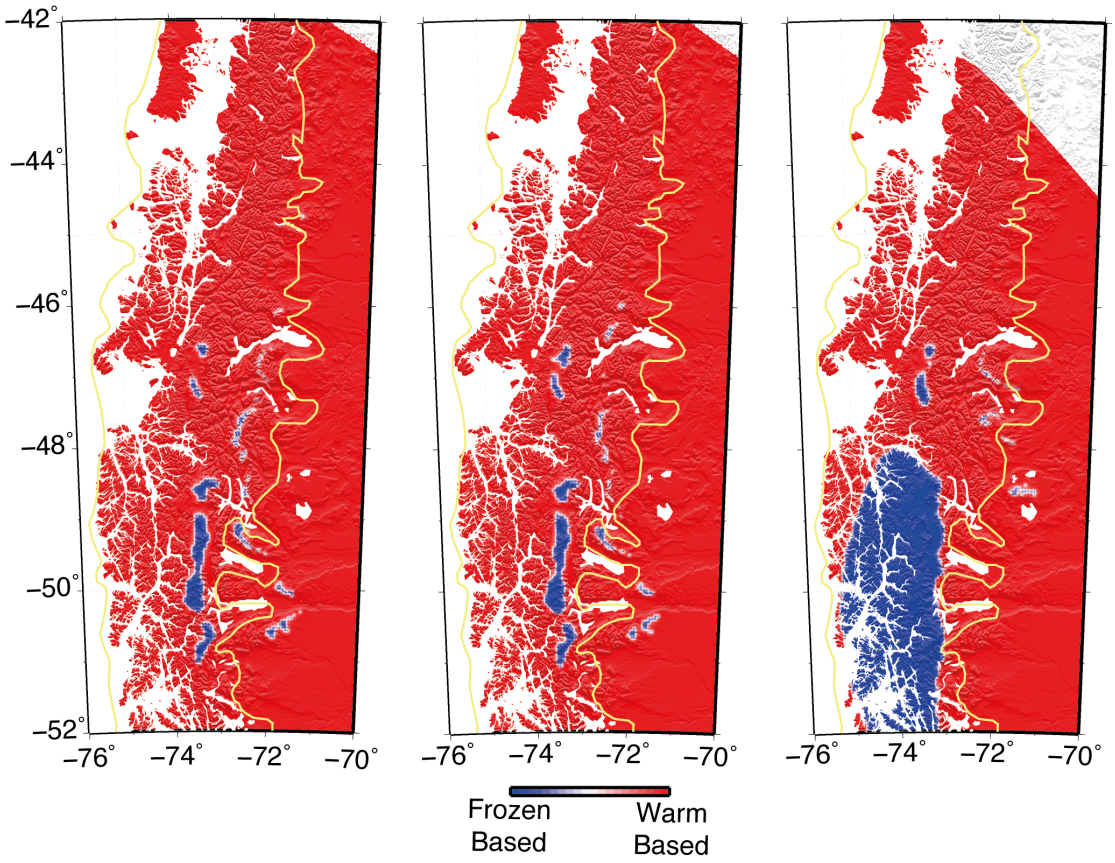

188

189 **Figure DR3. Basal temperature conditions.** The panels show where the ice is
190 frozen- or warm-based. The three panels correspond to the numerical
191 experiments shown in Figure 2.

192

193

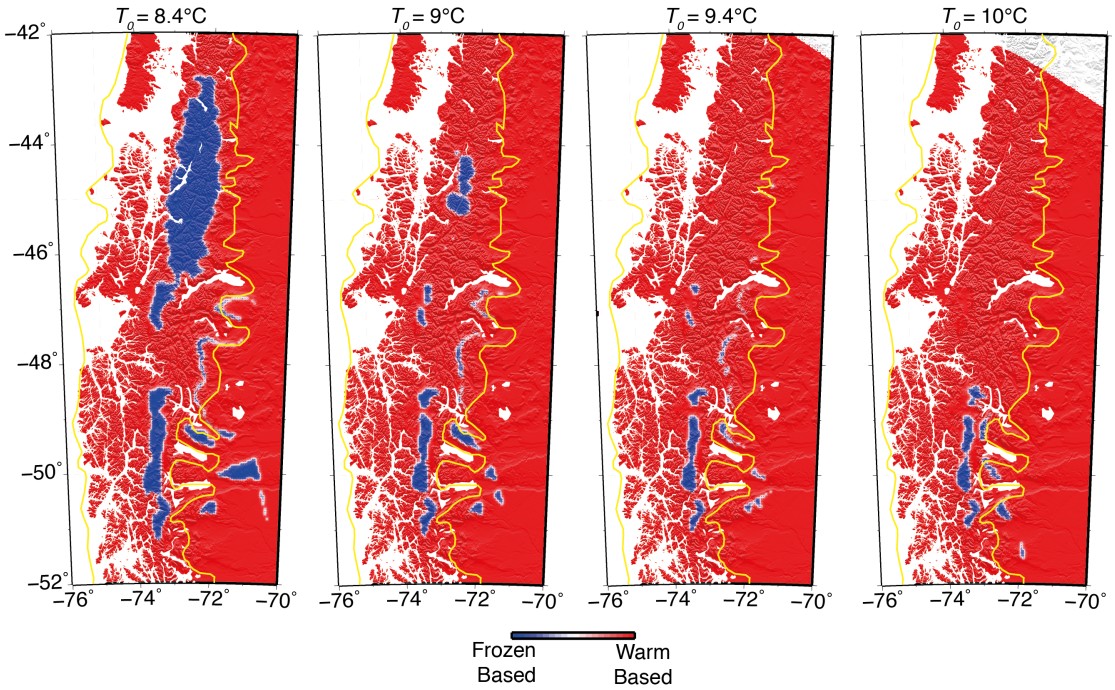

194

195 **Figure DR4. Basal temperature conditions for different surface**
196 **temperature conditions**. Each model corresponds to a different prescribed
197 value for T_0.

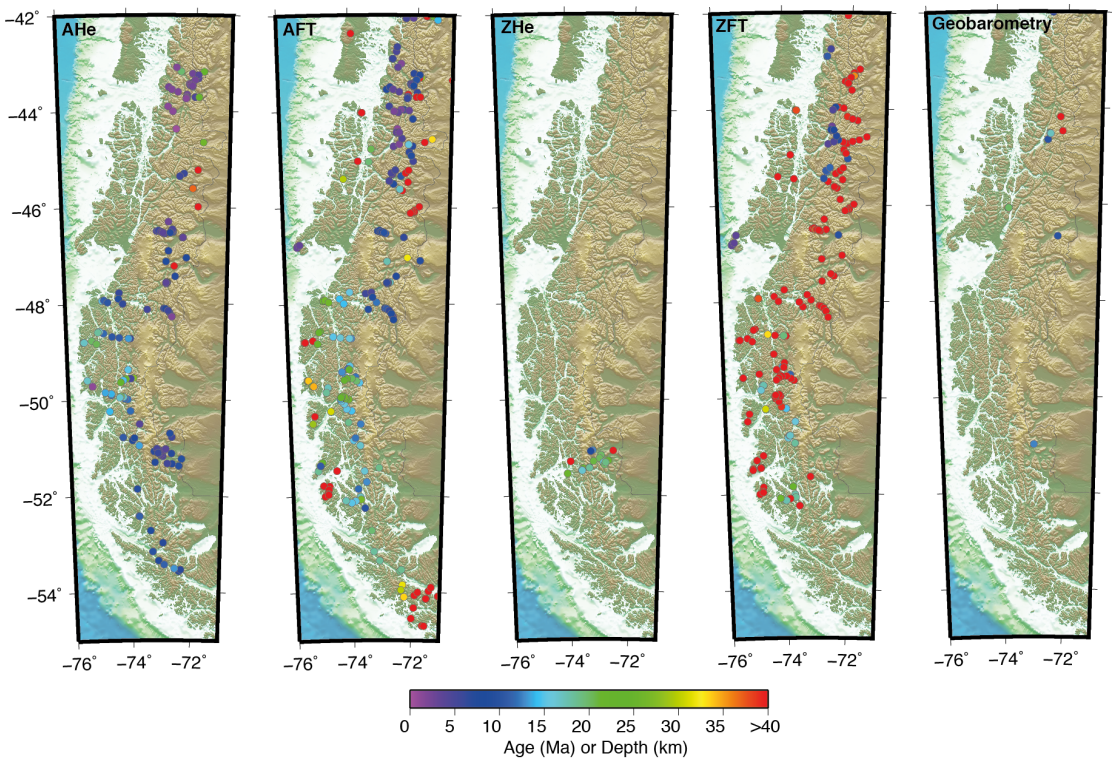

198

199 **Figure DR5. Thermochronometric and geobarometric data.**

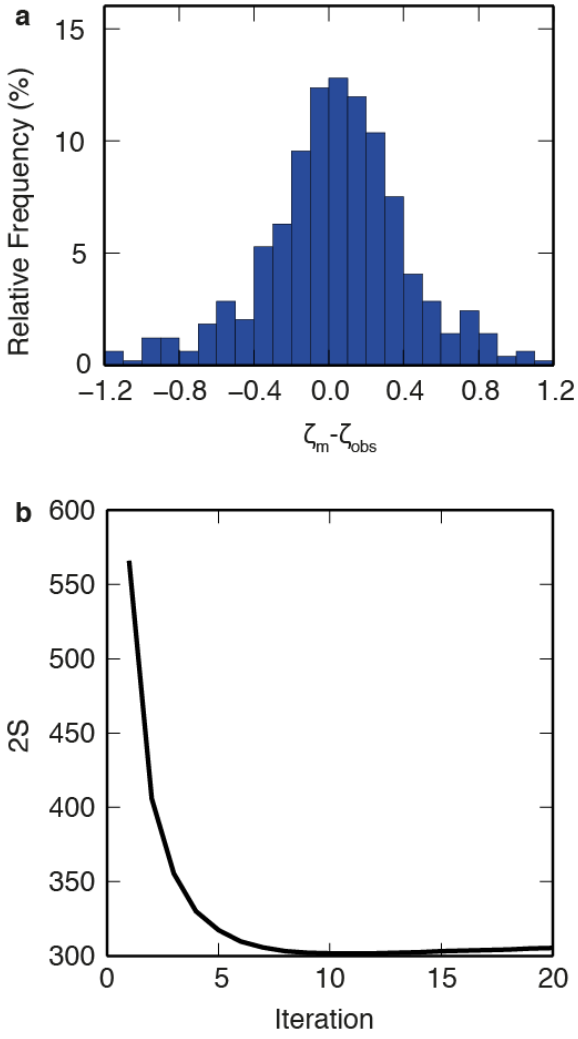

200
201

202 **Figure DR6. Inversion residuals.** The standard error on the residuals is nearly
203 twice smaller than the data standard error. *2S* corresponds to χ^2, and the degree
204 of freedom is set by the amount of data used in the inversion (Tarantola 2005,
205 p.74), i.e. 495. (To avoid computing the inverse of the covariance matrix, we only
206 include the diagonal terms, which lead to a slight underestimation of the χ^2. The
207 actual reduced $\chi^2$is close to 1.)

208

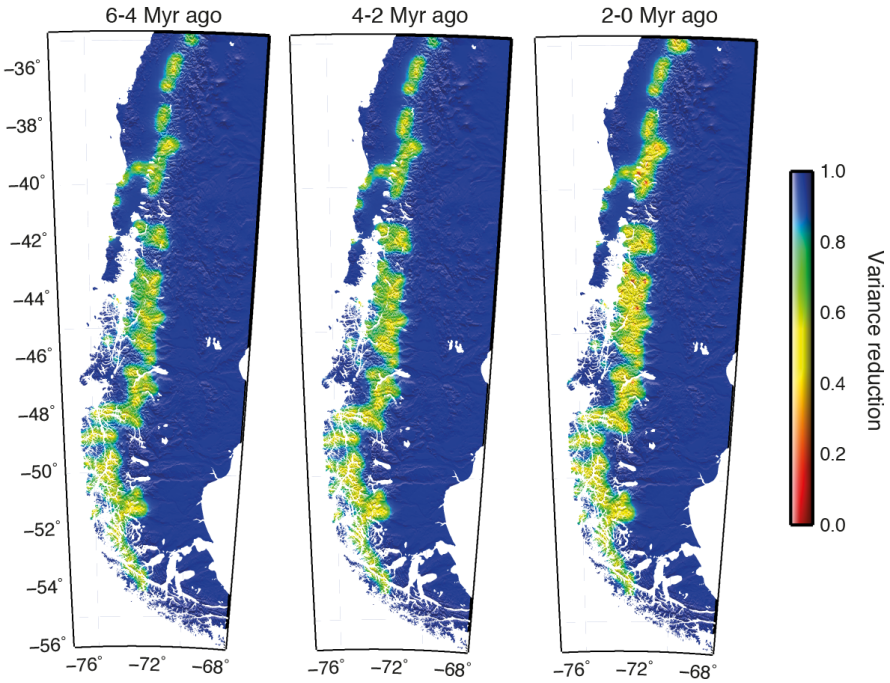

Figure DR7. Variance reduction. The panels show the variance reduction, i.e. ratio between a posteriori and a priori standard deviations, σ/σ_{po}, for the last 6 Myr.

Data Repository References

Aster, R., Borchers, B.& Thurber, C. Parameter Estimation and Inverse Problems 2nd edn (Elsevier, 2012).

Auer, A. H. Jr. The rain versus snow threshold temperatures. *Weatherwise* ***27*****(2)**, 67–67 (1974).

Clapperton, C. M. The quaternary glaciation of Chile: a review. *Revista Chilena De Historia Natural*, ***67*****(4)**, 369–383 (1994).

Clarke, G. K., Nitsan, U., & Paterson, W. Strain heating and creep instability in glaciers and ice sheets. *Reviews of Geophysics* **15(2)**, 235–247 (1977).

Cuffey K.M. & Paterson W.S.B. The Physics of Glaciers 4th edn. (Butterworth-Heinemann/Elsevier, 2010).

Fox, M., Herman, F., Willett, S. D., & May, D. A. A linear inversion method to infer exhumation rates in space and time from thermochronometric data. *Earth Surface Dynamics* ***2*****(1)**, 47–65 (2014).

Giesen, R. H., & Oerlemans, J. Global application of a surface mass balance model using gridded climate data. *The Cryosphere Discussions* ***6*****(2)**, 1445–1490 (2012).

Herman, F., Seward, D., Valla, P. G., Carter, A., Kohn, B., Willett, S. D., & Ehlers, T. A. Worldwide acceleration of mountain erosion under a cooling climate. *Nature* **504**, 423–426 (2013).

Hervé, F., Pankhurst, R. J., Demant, A., & Ramirez, E. Age and Al-in-Hornblende geobarometry in the north patagonian batholith, Aysen, Chile. (Third ISAC St Malo, 1996).

Hulton, N. R., Purves, R. S., McCulloch, R. D., Sugden, D. E., & Bentley, M. J. The last glacial maximum and deglaciation in southern South America. *Quaternary Science Reviews*, ***21*****(1)**, 233–241 (2002).

Humphrey, N. F., & Raymond, C. F. Hydrology, erosion and sediment production in a surging glacier: Variegated Glacier, Alaska, 1982-83. *Journal of Glaciology*, *40*(136), 539–552 (2010).

Hutter K. Theoretical Glaciology: Material Science of Ice and the Mechanics of Glaciers and Ice Sheets. (Reidel, 1983).

Leuthold, J., Müntener, O., Baumgartner, L. P., Putlitz, B., Ovtcharova, M., &

Schaltegger, U. Time resolved construction of a bimodal laccolith (Torres del Paine, Patagonia). *Earth and Planetary Science Letters* **325**, 85–92 (2012).

Moreno, P. I., Lowell, T. V., Jacobson Jr, G. L., & Denton, G. H. (1999). Abrupt Vegetation and Climate Changes During the Last Glacial Maximum and Last Termination in The Chilean Lake District: A Case Study from Canal De La Puntilla (41° S). *Geografiska Annaler: Series A, Physical Geography*, ***81*(2)**, 285-311.

Mahaffy, M. W. A three-dimensional numerical model of ice sheets: Tests on the Barnes Ice Cap, Northwest Territories. *Journal of Geophysical Research* **81(6)**, 1059–1066 (1976).

Oerlemans, J. Climate sensitivity of Franz Josef Glacier, New Zealand, as revealed by numerical modeling. *Arctic and Alpine Research* **29**, 233–239 (1997).

Porter, S. C. Pleistocene glaciation in the southern Lake District of Chile. *Quaternary Research*, ***16*(3)**, 263–292 (1981).

Robin, G. Ice movement and temperature distribution in glaciers and ice sheets. *Journal of Glaciology* **2(18)**, 523–532 (1955).

Rojas, M., Moreno, P., Kageyama, M., Crucifix, M., Hewitt, C., Abe-Ouchi, A., Ohgaito, R., Brady, E.C, & Hope, P. (2009). The Southern Westerlies during the last glacial maximum in PMIP2 simulations. *Climate Dynamics*, *32*(4), 525-548.

Seifert, W., Rosenau, M, Echtler, H. Crystallization depths of granitoids of South Central Chile estimated by Al-in-hornblende geobarometry: implications for mass transfer processes along the active continental margin. *Neues Jahrbuch für Geologie und Paläontologie, Abhandlungen* **236**, 115-127 (2005).

Tarantola, A. Inverse Problem Theory (SIAM, 2005).